ADVANCING EARTH AND SPACE SCIENCE

JGR Solid Earth

RESEARCH ARTICLE
10.1029/2022JB025993

Disruptive Role of Vertical Land Motion in Future Assessments of Climate Change-Driven Sea-Level Rise and Coastal Flooding Hazards in the Chesapeake Bay

Sonam Futi Sherpa[1,2], Manoochcher Shirzaei[1,2], and Chandrakanta Ojha[3]

[1]Department of Geosciences, Virginia Tech, Blacksburg, VA, USA, [2]Virginia Tech National Security Institute, Blacksburg, VA, USA, [3]Department of Earth and Environmental Sciences, IISER Mohali, Mohali, India

Key Points:

- We quantify 21st-century inundation hazards due to sea-level rise (SLR), storm surge, and land subsidence by combining space-based techniques
- By 2100, inundated areas from SLR, vertical land motion and storm surge increase to 849(832–867)–1,117(1,054–1,205) km^2 for Shared Socioeconomic Pathways 1–1.9 to 5–8.5
- Islands, wetlands, and national wildlife refuges flooded in even very low and low emissions scenarios such as SSPs 1–1.9 to 1–2.6

Supporting Information:

Supporting Information may be found in the online version of this article.

Correspondence to:

S. F. Sherpa,
sfsherpa@vt.edu

Citation:

Sherpa, S. F., Shirzaei, M., & Ojha, C. (2023). Disruptive role of vertical land motion in future assessments of climate change-driven sea-level rise and coastal flooding hazards in the Chesapeake Bay. *Journal of Geophysical Research: Solid Earth*, *128*, e2022JB025993. https://doi.org/10.1029/2022JB025993

Received 4 NOV 2022
Accepted 26 MAR 2023

Author Contributions:

Conceptualization: Sonam Futi Sherpa, Manoochcher Shirzaei
Data curation: Chandrakanta Ojha
Formal analysis: Sonam Futi Sherpa
Funding acquisition: Sonam Futi Sherpa, Manoochcher Shirzaei
Investigation: Sonam Futi Sherpa, Manoochcher Shirzaei, Chandrakanta Ojha
Methodology: Sonam Futi Sherpa
Resources: Sonam Futi Sherpa, Chandrakanta Ojha
Software: Sonam Futi Sherpa

Abstract Future projections of sea-level rise (SLR) used to assess coastal flooding hazards and exposure throughout the 21st century and devise risk mitigation efforts often lack an accurate estimate of coastal vertical land motion (VLM) rate, driven by anthropogenic or non-climate factors in addition to climatic factors. The Chesapeake Bay (CB) region of the United States is experiencing one of the fastest rates of relative sea-level rise on the Atlantic coast of the United States. This study uses a combination of space-borne Interferometric Synthetic Aperture Radar (InSAR), Global Navigation Satellite System (GNSS), Light Detecting and Ranging (LiDAR) data sets, available National Oceanic and Atmospheric Administration (NOAA) long-term tide gauge data, and SLR projections from the Intergovernmental Panel on Climate Change (IPCC), AR6 WG1 to quantify the regional rate of relative SLR and future flooding hazards for the years 2030, 2050, and 2100. By the year 2100, the total inundated areas from SLR and subsidence are projected to be 454(316–549)–600(535–690) km^2 for Shared Socioeconomic Pathways (SSPs) 1–1.9 to 5–8.5, respectively, and 342(132–552)–627(526–735) km^2 only from SLR. The effect of storm surges based on Hurricane Isabel can increase the inundated area to 849(832–867)–1,117(1,054–1,205) km^2 under different VLM and SLR scenarios. We suggest that accurate estimates of VLM rate, such as those obtained here, are essential to revise IPCC projections and obtain accurate maps of coastal flooding and inundation hazards. The results provided here inform policymakers when assessing hazards associated with global climate changes and local factors in CB, required for developing risk management and disaster resilience plans.

Plain Language Summary The Chesapeake Bay (CB) region of the United States is experiencing one of the fastest rates of relative sea-level rise on the Atlantic coast of the United States. However, future projections of sea-level rise (SLR) used to assess coastal flooding hazards and exposure throughout the 21st century often lack an accurate estimate of changes in land elevation. This poses a significant challenge to present and future management efforts because vertical land motion (VLM) can cause underestimation/overestimation of flooding risk to coastal communities. This work combines satellite data and in situ observations to measure VLM and assess 21st-century flooding hazards due to SLR, hurricane effect, and land elevation change in the CB. By the year 2100, the total inundated areas from SLR and subsidence are projected to be 454–600 km^2 for very low to very high greenhouse gas scenarios. The effect of storm surges associated with Hurricane Isabel can increase the inundated area to 849–1,117 km^2 under different SLR scenarios and VLM. The results provided here inform policymakers when assessing hazards associated with global climate changes and local factors.

1. Introduction

Rising sea levels pose significant challenges to coastal communities and ecosystems (IPCC, 2021). The global sea level rose by 0.20 m between 1901 and 2018, with an average rate of 1.3 mm/year between 1901 and 1971, increasing to 1.9 mm/year between 1971 and 2006 and further increasing to 3.7 mm/year between 2006 and 2018 with high confidence (IPCC, 2021). This acceleration will likely continue throughout the 21st century (Dangendorf et al., 2019; Frederikse et al., 2020; Nerem et al., 2018). However, on a local scale, the rate of regional sea-level change could be larger than the average global sea-level change due to processes that affect vertical land motions (VLMs) such as groundwater pumping/recharge, sediment compaction, hydrologic loading, long-term tectonics, glacial isostatic adjustment (GIA), dynamic topography, and sediment loading (Shirzaei et al., 2021) alongside thermal expansion, ocean dynamics, and Greenland ice mass loss (Davis & Vinogradova, 2017). Relative

Supervision: Manoochcher Shirzaei
Validation: Sonam Futi Sherpa
Visualization: Sonam Futi Sherpa
Writing – original draft: Sonam Futi Sherpa
Writing – review & editing: Sonam Futi Sherpa, Manoochcher Shirzaei

sea-level change refers to sea surface changes over time concerning a local land elevation in response to changing climate and nonclimatic processes. To quantify the impacts of relative sea-level rise (RSLR) on coastal flooding, socioeconomic exposures, and risks, it is crucial to obtain accurate VLM rates at management-relevant resolution (10s of meter square (m^2)) (Blackwell et al., 2020; Shirzaei & Bürgmann, 2018).

Several studies have highlighted sea-level rise (SLR) in coastal Virginia waters and have identified it as a hotspot for rising sea levels due to climate variability and global warming (Davis & Vinogradova, 2017; Ezer & Corlett, 2012; Sallenger et al., 2012). On the land side, recent studies (Bekaert et al., 2017; Buzzanga et al., 2020; Harvey et al., 2021; Karegar et al., 2017) showed that the Hampton Roads area of the Chesapeake Bay (CB) region (Figure 1) is experiencing subsidence and suggested GIA and aquifer compaction as primary drivers (Eggleston & Pope, 2013). The mid-Atlantic region's bedrock is slowly moving downward in response to the melting of the Laurentide Ice Sheet that covered Canada and the northern United States during the last ice age (Boon et al., 2010; Sella et al., 2007), generating ∼1–2 mm/year of subsidence (Peltier et al., 2018). Further, the region hosts the Coastal Plain Aquifer system comprising unconsolidated sediments overlaying the eastward dipping Precambrian basement (McFarland & Scott, 2006). The Potomac Aquifer, the largest and deepest unit among different layers, is the primary source of freshwater supply in eastern Virginia. As a result, pumping has caused the groundwater level to decline by >60 m in some regions, manifesting in localized and rapid land subsidence (Bekaert et al., 2017). Currently, the Sustainable Water Initiative for Tomorrow (SWIFT) (https://www.hrsd.com/swift) project designed by Virginia authorities actively recharge replenishes the Potomac Aquifer with up to 1 million gallons (∼3,785,411 L) of drinking water daily to enhance freshwater's long-term sustainability and offset the land subsidence.

CB region is affected by combined flooding from ocean dynamics of the Gulf Stream and Atlantic Meridional Overturning Circulation (Ezer & Corlett, 2012), tidal flooding (Sweet & Park, 2014), and documented increasing extreme rainfall (Allen & Allen, 2019). On the other hand, increased inundation hazards due to storm surges in the CB are demonstrated in various studies (Cho et al., 2012; Shen et al., 2006; Sheng et al., 2010). On 18 September 2003, a category 2 Hurricane Isabel (return period of 52–105 years in regions of CB) made landfall over the mid-Atlantic region, generating record conditions for the region's 27 years of monitoring and impact (Smith & Graffeo, 2005), resulting in a historical maximum water level records at eight stations in the CB (Hovis et al., 2004). On 2012 October 29, Hurricane Sandy (category 1) (return period of 52–105 years), an Atlantic hurricane on record, made landfall on a long swath of the US Atlantic coastline, including the CB (Sopkin et al., 2014) with a damaging storm surge imparted to the New Jersey and New York coastlines (Blake et al., 2013). The maximum recorded storm surge from National Oceanic and Atmospheric Administration (NOAA) ranked by amplitude for Hurricane Isabel, September 2003 and Hurricane Sandy, October 2012 is reported in Table S1 of Supporting Information S1, which shows that Sewell's Point, Cape May station, and Washington DC experienced a water level of 1.7, 1.0, and 2.4 m (for Hurricane Isabel) and 1.4, 1.6, and 1.2 m, respectively (for Hurricane Sandy). Further, some areas, such as the City of Norfolk, regularly experience "sunny days" or nuisance flooding when there is a high tide or a storm offshore, without a named storm event on land. These increasingly frequent flooding events will require regional and local planning for evacuations in the face of extreme storm events and longer-term adaptation. In the CB, a study by Sweet and Park (2014) reported acceleration in the annual exceedances that impinge on the flood threshold coming from the growth of tidal water level distribution to a higher elevation, suggesting a tipping point for coastal inundation and more in 21st century. Further, SLR has resulted in a long-term erosion of barrier beaches on the east coast, which had maintained a state of dynamic equilibrium due to the existence of barrier islands regardless of storm severity (Zhang et al., 2004). This makes the CB a significant region worldwide, and a hotspot for SLR impacts to learn from and plan accordingly for future.

Space geodetic tools, including Interferometric Synthetic Aperture Radar (InSAR) and Global Navigation Satellite System (GNSS), can measure the movement of the land surface at a millimeter-level accuracy (Bürgmann et al., 2000), which is essential in understanding change in relative SLR rate. Such observations improve the understanding of long-term changes in relative sea level. The usefulness of space-based InSAR and GNSS observation are discussed in various studies on earth deformation in the CB (Bekaert et al., 2017; Buzzanga et al., 2020). However, these studies only focused on short observation periods spanned by Advanced Land Observing Satellite (ALOS) or a portion of Sentinel-1 A/B acquisitions, thus yielding a lower accuracy for the long-term rates. Also, their estimates of the VLM rate are not tied to a reference frame, so they are unsuitable for studies of SLR and flooding hazards.

We apply an advanced multitemporal algorithm to combine the entire archive of Sentinel-1 and ALOS SAR satellites and GNSS observations to span more than a decade of land elevation change in the region and obtain spatially

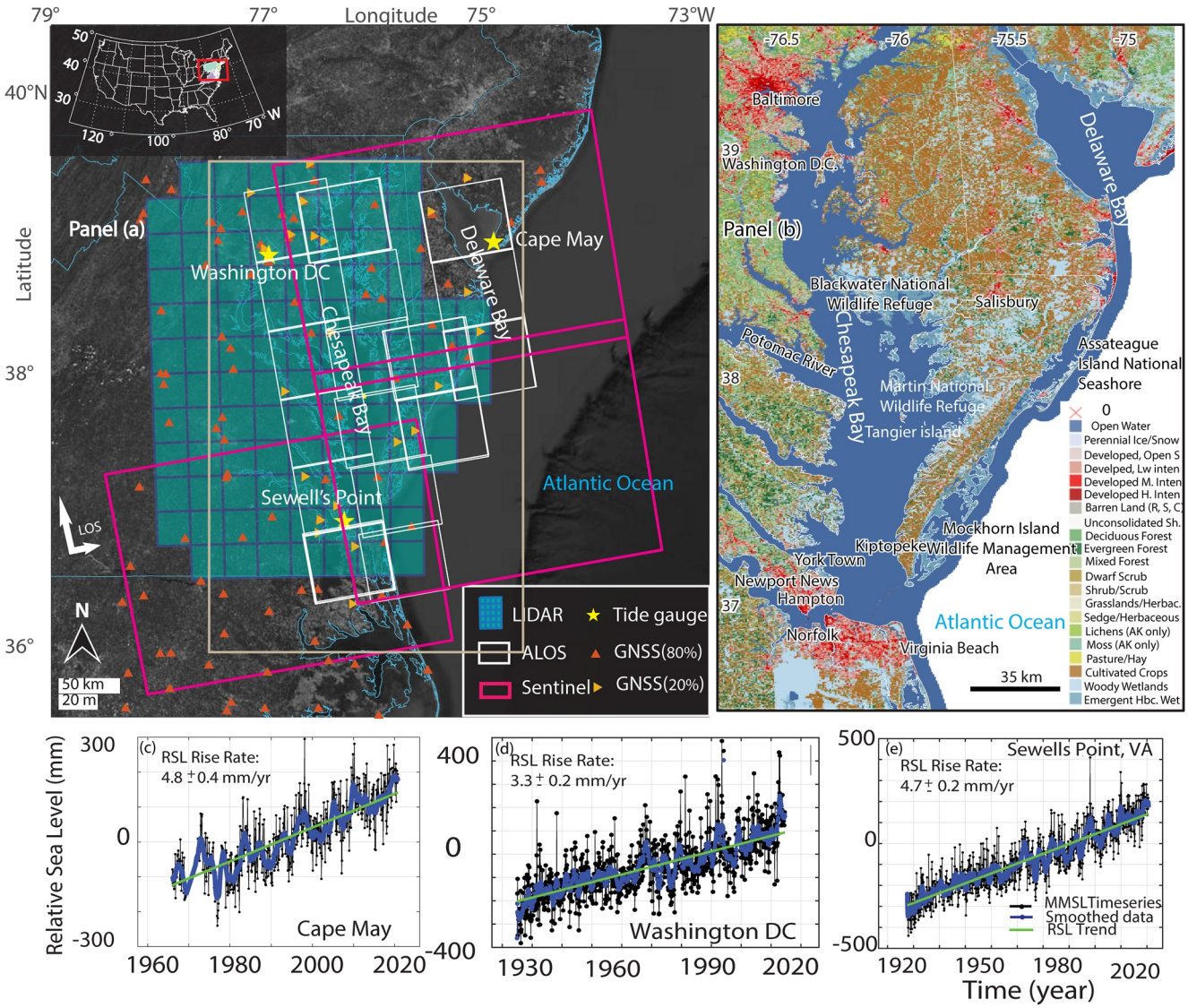

Figure 1. Chesapeake Bay study area. (a) shown are the ground footprint of SAR satellites frames, Sentinel-1 A/B, C-band (Magenta) and Advanced Land Observing Satellite PALSAR L-band (white), location of tide gauges (yellow stars), Global Navigation Satellite System (GNSS) tie stations (80%) used in the analysis (orange triangle) and 20% of GNSS check stations (yellow triangles) used for VLM validation. (b) Landsat-based 30-m resolution land use and land cover area for the study area (source: Homer et al., 2012, USGS). (c–e) Time series data of monthly mean sea level (MMSL) (average of high tides and low tides) from NOAA (National Oceanic and Atmospheric Administration) for three stations, Sewell's Point, VA, Washington DC, and Cape May.

and temporally high-resolution long-term VLM maps and improve their uncertainties. The availability of these data sets enables the first comprehensive evaluation of future flooding and inundation hazards for the CB by combining VLM rates with the Light Detecting and Ranging (LiDAR) topographic data set, SLR projections under different Shared Socioeconomic Pathways (SSPs) scenarios, and storm surge height estimates from Hurricanes Sandy and Isabel for period 2030–2100. High-resolution VLM rates with mm-level accuracy, improved forecasts of relative SLR rates, and updated maps of inundation hazards are essential for informing policymakers and authorities and developing flood resiliency plans to combat severe consequences of climate change in the region.

2. Data Sets and Methods

2.1. Tide Gauge Data

We used NOAA tide gauges to understand the water level changes in the CB (Figures 1c–1e). The tide gauge data were obtained from the NOAA website https://tidesandcurrents.noaa.gov/map/index.html. Water level

measurements with record lengths varying between 93 years (1927–2020) at Sewell's Point (8638610), VA, 96 years (1924–2020) at the Washington DC station (8594900), and 55 years (1965–2020) at the Cape May site (8536110) are available. The monthly mean sea level (MMSL) heights recorded at the US tide stations are verified for their accuracy through National Water Level Observation Network (NWLON) quality control procedures. They are referenced to *mean sea level* (MSL), a tidal datum specifically defined in and for the US following Federal law (Gill & Schultz, 2001). Linear trend analysis of the MMSL data from these three stations adjacent to or within SAR frames showed a relative sea level of 4.7 ± 0.2 mm/year at Sewell's Point, 3.3 ± 0.2 mm/year, and 4.8 ± 0.4 mm/year at Washington DC and Cape May stations, respectively (Figures 1c–1e). Comparatively, tide gauge at Washington DC observes a lesser subsidence rate (therefore, lower RSLR) than tide gauge location at Sewell's Point. A study by Boon (2018) has also shown increasing regional sea level using a quadratic model among coastal regions. The MMSL data refer to the water level observed over a calendar month at US tide stations.

2.2. SAR and GNSS Data Sets

To obtain a map of high-resolution VLM with respect to a global reference frame and mm-level precision, we applied the framework shown in Figure S1 in Supporting Information S1 to combine all available SAR and GNSS observations. To measure VLM in the CB, a large set of SAR images acquired by C-band Sentinel-1 with Terrain Observation with Progressive Scans (TOPS) acquisition mode (Interferometric Wide Swath-IW mode) during 2017–2020 with a revisit time of 12 days and the ALOS Phased Array L-band Synthetic Aperture Radar (PALSAR) with a revisit time of 46 days spanning 2007–2011 in ascending orbit geometry were used. The list of acquisitions is provided in Table D1 of Supporting Information S2. We used Gamma processing software (Wegnüller et al., 2016; Werner et al., 2000) to generate large sets of high-quality interferograms and applied Wavelet-based InSAR (WabInSAR) time series algorithm to identify elite pixels (i.e., distributed and permanent scatterers), correct for atmospheric errors and estimate line-of-sight (LOS) time series, rates, and uncertainties (Lee & Shirzaei, 2023; Shirzaei, 2013; Shirzaei et al., 2017) for each frame. Using the overlap areas of adjacent frames, we performed an affine transformation to combine respected frames and generate a seamless map of LOS velocity for Sentinel-1 and ALOS data sets (Blackwell et al., 2020). Assuming a sublinear surface deformation rate during 2007–2020, we combine LOS rates from ALOS, Sentinel-1, and GNSS 3D displacement fields to generate high-quality maps of 3D displacement fields for each elite pixel (Miller & Shirzaei, 2021). Further details on methods are provided online in Supporting Information S1.

2.3. GNSS Time Series Analysis

To investigate the decadal-scale linear versus nonlinear patterns in VLM across CB, we used vertical deformation time series from 144 GNSS stations that have data during 2000–2020 (Figure 2a). Next, using a 10-year moving window, we estimate the rates for each station (Figure 2b). Overall estimated windowed rates per station vary <0.1 cm/year (Figure 2c), indicating the sublinearity of the vertical motion within the study area for nearly two decades.

We further apply Singular Spectrum Analysis (SSA) to the VLM time series at selected GNSS stations with long observation duration. Given a time window of M, the SSA identifies nearly periodic so-called reconstructed components (RCs) with periods less than M and 1–2 less periodic RCs with a wavelength longer than M (Chen et al., 2013). Following Chen et al. (2013), we chose $M = 3$ years and extracted the RCs of long wavelengths. Figures 2d–2f show the original observations and the sum of the RCs 1 and 2 obtained from SSA analysis. The sublinear trend of RCs is evident.

2.4. LiDAR Data Set

Next, we obtained a LiDAR elevation model with a 1-m × 1-m resolution for CB from the United States Geological Society (OCM Partners, 2021; Figure S2c in Supporting Information S1). The 2016 USGS CoNED (Coastal National Elevation Database) Topo bathymetric Model (1859–2015): CB data sets were obtained as a raster digital elevation model with vertical accuracy of 30 cm and horizontal accuracy of 100 cm with vertical Datum NAVD88 (North American Vertical Datum of 1988). This data has a temporal range of the input topography of 1859–2015. The VLM rates obtained in Section 2.2 are resampled on this LiDAR DEM which is referred to as

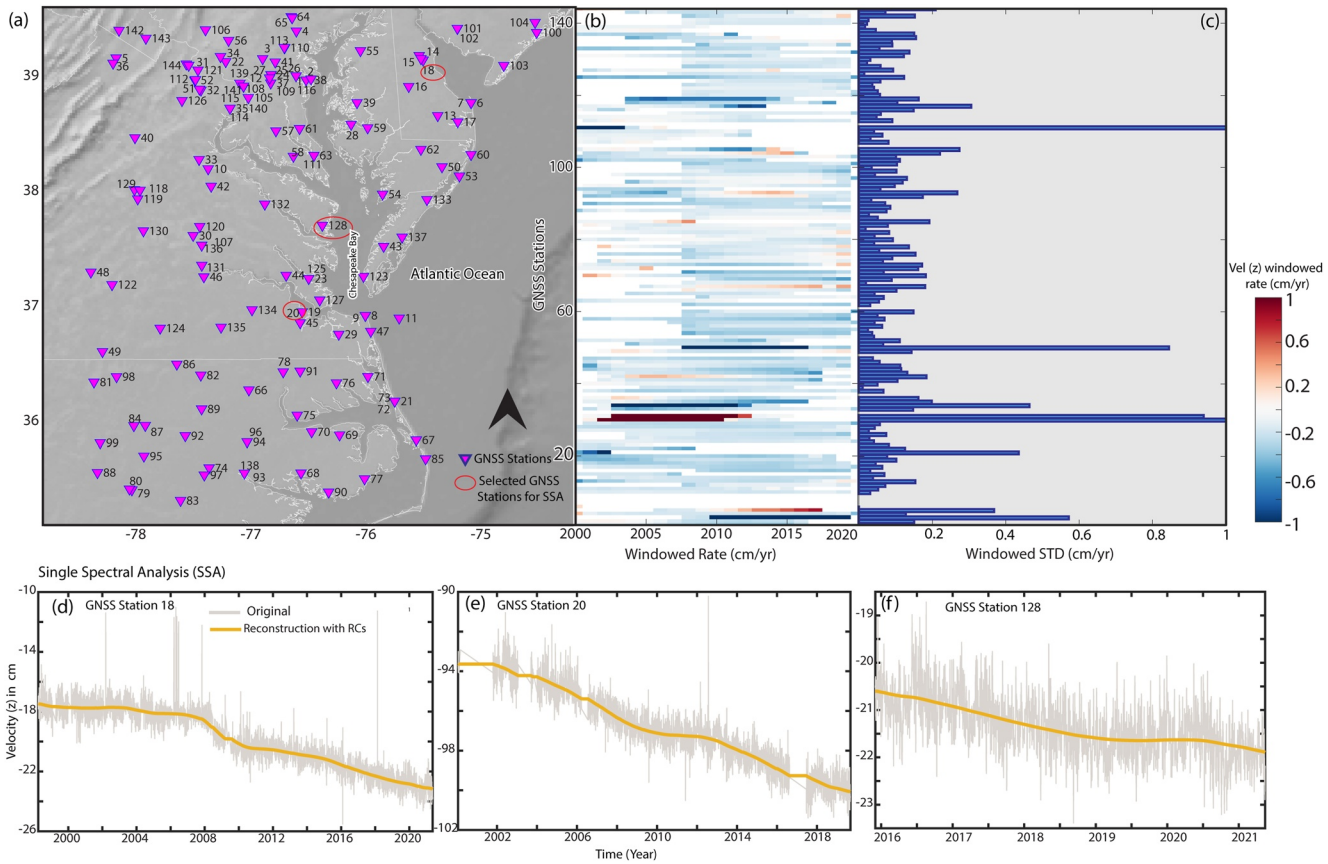

Figure 2. (a) Location of GNSS stations within the study area, stations are labeled with a number used in panels (b) and (c). (b) VLM rate variations per GNSS station from analyzing vertical time series within a moving window of 10 years for 2000–2020. (c) Temporal variation of the windowed VLM rate per station in terms of standard deviation. (d–f) Singular Spectrum Analysis (SSA) of VLM time series of selected GNSS stations 18, 20, and 128 with ∼20 years of observations locations (d and e) and ∼7 years (f) marked in panel (a). Detail of GNSS stations including labels, latitudes, and longitudes is provided in Table D2 of Supporting Information S2.

the same coordinate system. We then adjust the DEM to incorporate a linear projection of subsidence during the 21st century (IPCC, 2021; Shirzaei et al., 2021).

We next subject the adjusted elevation model for VLM linear projections to multiple SLR and storm surge scenarios by subtracting the height of the transformed DEM (Figure S2c in Supporting Information S1) from the SLR projection height. A similar approach is used by Miller and Shirzaei (2021). We consider all the areas with elevation lower than the water level as flooded in the case of storm surge (Hinkel et al., 2014). This approach may overestimate the flooded area as it does not account for runoff and soil infiltration.

2.5. IPCC SLR Scenarios From AR6

We use future SLR scenarios from the latest Sixth Assessment Report (AR6; Fox-Kemper et al., 2021; Garner et al., 2021) following SSPs (O'Neill et al., 2014; Riahi et al., 2017) adopted by the IPCC for projection periods of 2030, 2050 and 2100, relative to a baseline of 1995–2014 with medium confidence and low confidence. In AR6 scenarios, a broader range of emissions futures is covered than considered in the Fifth Assessment Report, AR5, including high CO_2 emissions scenarios without climate change mitigation and a low CO_2 emissions scenario reaching net-zero CO_2 emissions around midcentury (Arias et al., 2021). SSPs scenarios offer a more comprehensive assessment of climate drivers and responses and offer unprecedented detail of input data for Earth System Model (ESM) simulations than in the Representative Concentration Pathways (RCPs) used in the AR5 (Arias et al., 2021).

SLR projections account for contributions from global processes such as melting of the Greenland Ice Sheet (GIS), Antarctic Ice Sheet (AIS), land water storage changes, and sterodynamic processes, as well as long-wavelength

VLM signals due to GIA. A detailed description of the process is found in IPCC AR6 report Box 9.1 (Fox-Kemper et al., 2021). We use the 50th percentiles (i.e., median) and likely ranges (i.e., lower, 17th percentile and upper, 83th percentile) projections for different SLR scenarios of SSP 1–1.9, SSP 1–2.6, SSP 2–4.5, SSP 3–7.0, and SSP 5–8.5 at the location of three tide gauge stations within the CB area, including Sewell's Point, Cape May, and Washington DC (Tables S2 and S3 in Supporting Information S1) to investigate inundation hazards. Here, SSP 3–7.0 and SSP 5–8.5 indicate high and very high greenhouse gas (GHG) emissions and CO_2 emissions that will roughly double from current levels by 2100 and 2050, respectively, SSP 2–4.5 is scenarios with intermediate GHG emissions and CO_2 emissions remaining around current levels until the middle of the century, and SSP 1–1.9 and SSP 1–2.6 represent scenarios with very low and low GHG emissions and CO_2 emissions declining to net zero around or after 2050, followed by varying levels of net negative CO_2 emissions (IPCC, 2021, Summary for Policy Maker, Box SPM 1).

For our analysis, we obtained the SLR projections without the effect of VLM as well as SLR due only to the effect of VLM. The former is used in combination with our measured VLM rates to investigate inundation hazards in the region, while the latter is used to assess the accuracy of VLM rates used in the IPCC projections compared to our observed VLM.

2.6. Storm Surge Estimates

We obtained recorded storm surge levels for Hurricane Isabel (Hovis et al., 2004) and Hurricane Sandy (Fanelli et al., 2013) in September 2003 and October 2012, respectively, to create inundation scenarios due to SLR and storm surges, assuming that Sandy and Isabel-like surges are likely to occur in the future (Lin et al., 2012). Here storm surge is defined as the local change in the elevation of the ocean along a shore due to a storm and represents the observed water level/storm tide-minus predicted astronomical tide levels, e.g., water motion which would result from Earth's rotation and gravitation effects following NOAA report (Fanelli et al., 2013; Hovis et al., 2004). Recorded details on storm surge levels, dates, and times from Hurricanes Sandy and Isabel used for our analysis for flood inundation can be found in Table S1 of Supporting Information S1. We only evaluate the effect of storm surge on inundation hazards for the high reference scenario with no additional climate policy namely SSP 5–8.5 for SLR.

3. Results

3.1. VLM Rate and Validation

We obtained VLM for 2007–2020 after processing an extensive set of Sentinel-1 and ALOS SAR acquisitions and further estimated uncertainty in the rate (Figure 3). Over the CB, a spatially variable subsidence rate of up to −5.5 mm/year and a standard deviation of a maximum of 1.6 mm/year is observed. A few subsidence hotspots are highlighted in Figure 3. Panels (c–e) show Southern CB, Cape May, and Washington DC areas where tide gauge stations are located. The southern CB area, mainly the Hampton region and Newport News, is undergoing subsidence with -3 ± 0.4 to -4 ± 0.4 mm/year (Figure 3c). A lower subsidence rate is observed at the tide gauge of Washington DC (Figure 3e), likely cause of the lowers rate of SLR observed at this tide gauge (Figure 1d).

To validate the InSAR-based estimate of VLM, we use a subset of selected GNSS stations, comprising 20% of available stations, which were chosen randomly and were not used in our analysis and highlighted in Figure 3a with diamond shapes. We found a good agreement between the data set, with a standard deviation of 0.34 mm/year for the difference between InSAR-based VLM and GNSS vertical rate (Figures 3f and 3g). Further, horizontal velocity fields (east-west and north-south) and their validation against independent GNSS observations are shown in Figure S5 in Supporting Information S1. Small uplift signals are observed near Calvert County, Maryland, likely due to aquifer recharge, observed in the groundwater level measurement at sites Prince Frederick, MD (Figure S7a in Supporting Information S1) and Cover Point, MD (Figure S7b in Supporting Information S1) from 2017 to 2021.

3.2. Non-GIA Contributions

To examine the non-GIA contributions in the estimated VLM, we used the GIA ICE-6G-D model (Figure 4b) (Peltier et al., 2018) and removed its effect from the observed VLM. VLM from the GIA model

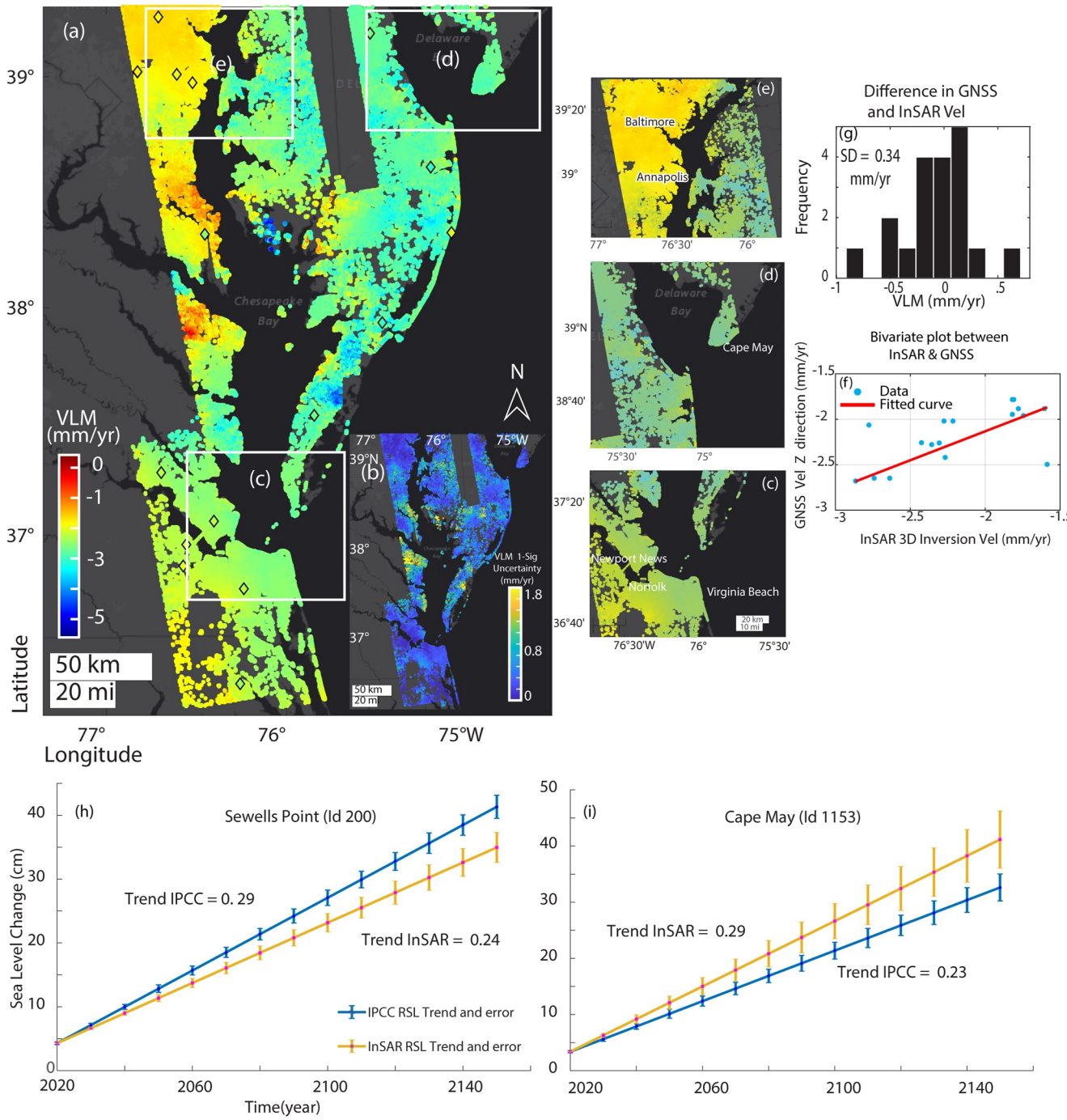

Figure 3. (a) Vertical land motion (VLM) rate (mm/year) over the Chesapeake Bay (CB) from 2007 to 2020 as a combination of Advanced Land Observing Satellite PALSAR, Sentinel-1A, and GNSS data sets. GNSS stations used for validation are highlighted in diamond and color-coded to their observed vertical rates. (b) VLM 1σ standard deviation. Boxes (c)–(e) show three zoomed-in locations of the CB, highlighted in panel (a). The validation results between the 20% GNSS station data and the estimated VLM are conducted in panels (f) (mm/year) and (g). Comparison of sea-level change due to vertical land motion from IPCC Sixth Assessment Report, AR6, using median data sets (50th percentile) and comparison of sea-level change (in cm) from our VLM estimate, at three selected tide gauge stations (h) Sewell's Point and (i) Cape May. 1-sigma error is also shown for each station. The PSMSL (Permanent Service for Mean Sea Level) ID numbers are shown based on IPCC data sets (Garner et al., 2021).

projected on InSAR pixels (Figure 4a) shows a persistent collapsing forebulge of the Laurentide Ice Sheet in the study area with a median rate of −1.88 mm/year (and range of −2.14–1.36 mm/year). The InSAR-based VLM map exhibits a similar pattern but at a higher subsidence rate of up to −5 mm/year, as shown in Figure 4c. After removing the effect of GIA (Figures 4d and 4e) the VLM rate map mainly comprises the influence of non-GIA

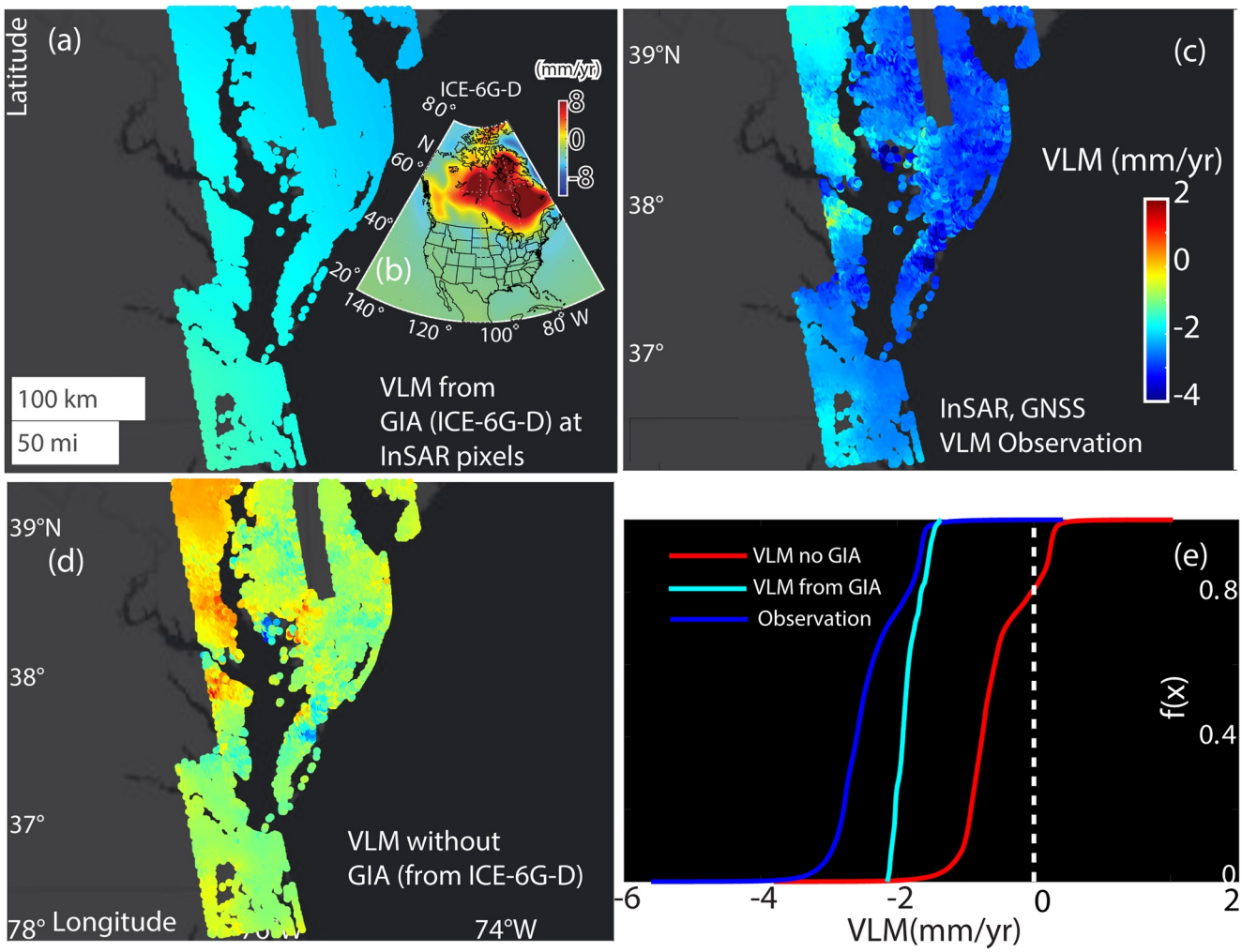

Figure 4. Vertical land motion (VLM) rate with and without the influence of glacial isostatic adjustment (GIA). (a) VLM from GIA oversampled on InSAR pixels, data from using ICE-6G-D model (b) (Peltier et al., 2018). (c) Estimated VLM in this study InSAR and GNSS, and VLM. (d) VLM rate after removing the effect of GIA. (e) Empirical cumulative distribution function for data sets shown in panels (a–d). Note that panels (a, c, and d) have same color bar.

contributions, including groundwater extraction and sediment compaction. We observe non-GIA subsidence rates as high as −4 mm/year in some areas, 2–3 times faster than long-term geologic rates, consistent with that reported in earlier studies (e.g., Karegar et al., 2016). Possible drivers of non-GIA subsidence include aquifer compaction due to groundwater pumping, evident from the region's declining groundwater levels, as shown in Figure S6 in Supporting Information S1. Also, the compaction of sediments under their weight can cause slow sublinear subsidence over a broad area (Jankowski et al., 2017; Zoccarato et al., 2018). We also found that some regions, mainly along the coastline, undergo non-GIA uplift up to 1 mm/year, corresponding with rebounding aquifers (Figure S7 in Supporting Information S1) and possibly aggrading wetlands (Jankowski et al., 2017; Zoccarato et al., 2018).

3.3. Comparison With IPCC VLM Projections

We compared linearly projected VLM information used in IPCC Sixth Assessment Report, AR6, considering its median estimates (50th percentile) with a linear projection of our VLM rates at two tide gauge stations (Figures 3h and 3i) till the 2150 time period from 2020. We note that the temporal evolution of VLM is often not linear (Shirzaei et al., 2021). However, in our study area, examining nearly two decades of GNSS observations (Figure 2) suggests that the rate of VLM remains steady at decadal scales, given the observation errors. For VLM at the tide gauge location, we selected pixels within a radius of 200 m and obtained the average rate. We found IPCC sea-level change from VLM projection was overestimated in Sewell's Point with a

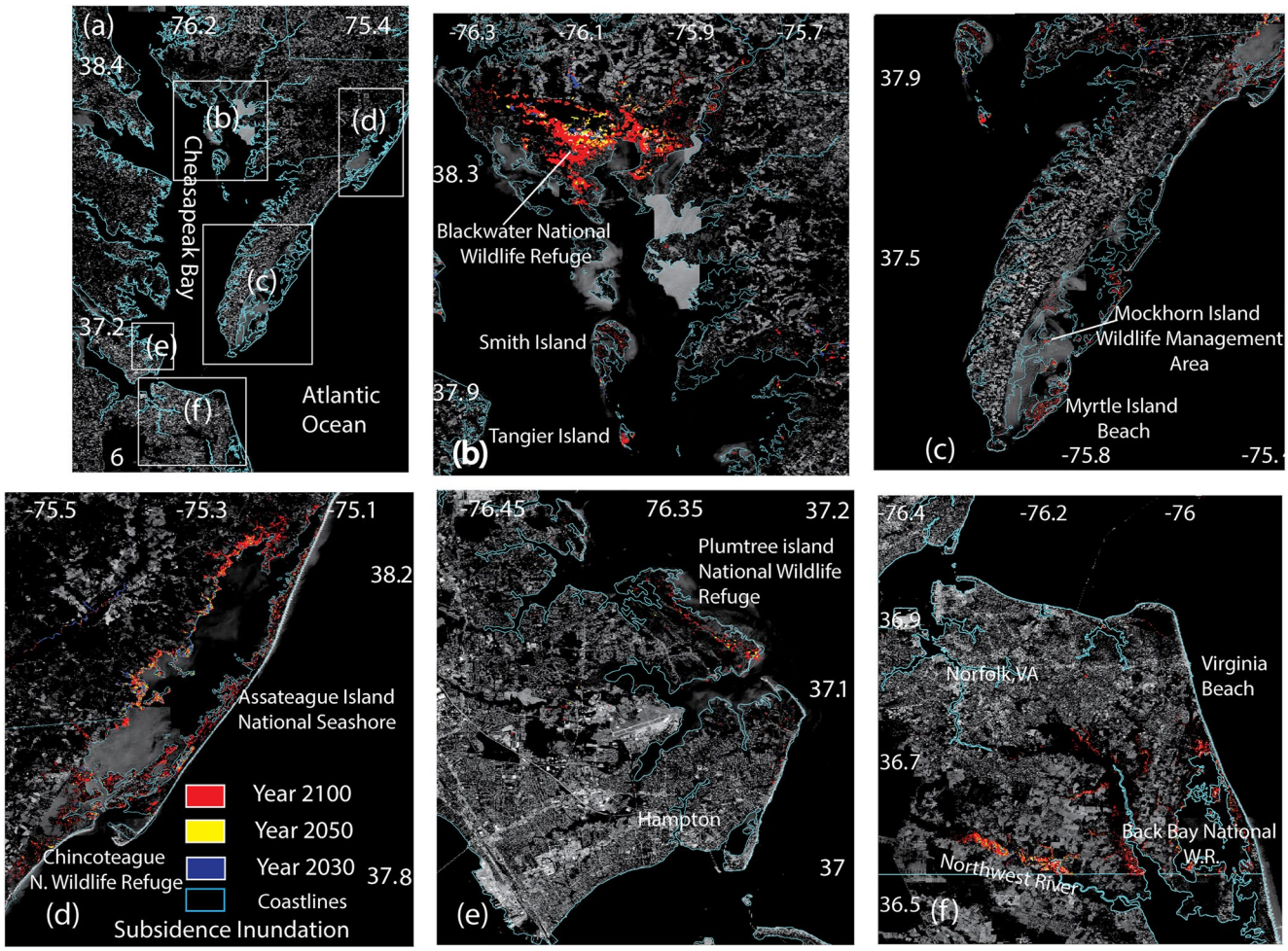

Figure 5. Projected inundation area from subsidence in years 2030, 2050, and 2100 using our vertical land motion measurement. Panel (a) shows the overview and panels (b)–(f) highlights the zoomed-in subsidence inundation for three-time scales.

value of 0.29 cm/year compared to our estimate of 0.24 cm/year and underestimated in Cape May with values of 0.23 cm/year versus 0.29 cm/year estimated here. This comparison highlights the need for incorporating high-resolution observation of VLM in future projections of SLR to obtain accurate estimates of future flooding and inundation hazards.

3.4. Projected Inundation Hazards

The projections of current VLM rates combined with LiDAR topographic data, SLR projection scenarios, and storm surge heights allow the evaluation of future inundation hazards. These projections are required to improve preparedness and have important implications for flood mitigation and resiliency. The projected inundation areas due to only VLM in three-time snapshots, 2030, 2050, and 2100 are shown in Figure 5, indicating increasing inundation near the wildlife reserve and coastal plains area. Inundation projections from SLR and VLM at climate scenarios, SSP 1–1.9 and SSP 5–8.5 at 3-time scales (2030–2050–2100) (medium confidence, median values) are shown in Figures 6 and 7, SSPs 1–2.6, 2–4.5, and 3–7.0 are shown in Figures S8–S10 in Supporting Information S1, SLR inundation for 2100 time period for all SSPs in Figure S11 in Supporting Information S1. Figure 8 shows the projected inundation area from both subsidence, SLR, and storm surge at SSP 5–8.5 for time scales 2030, 2050, and 2100 for Hurricanes Isabel and Sandy, respectively (at medium confidence) and inundated area (km^2) from all scenarios are shown in Figure 9.

Further, projected inundated area from VLM and SLR under climate scenarios, SSP 1–1.9 and SSP 5–8.5 at 3-time scales (2030–2050–2100) (medium confidence) and incorporating storm surge at SSP 5–8.5 likely ranges,

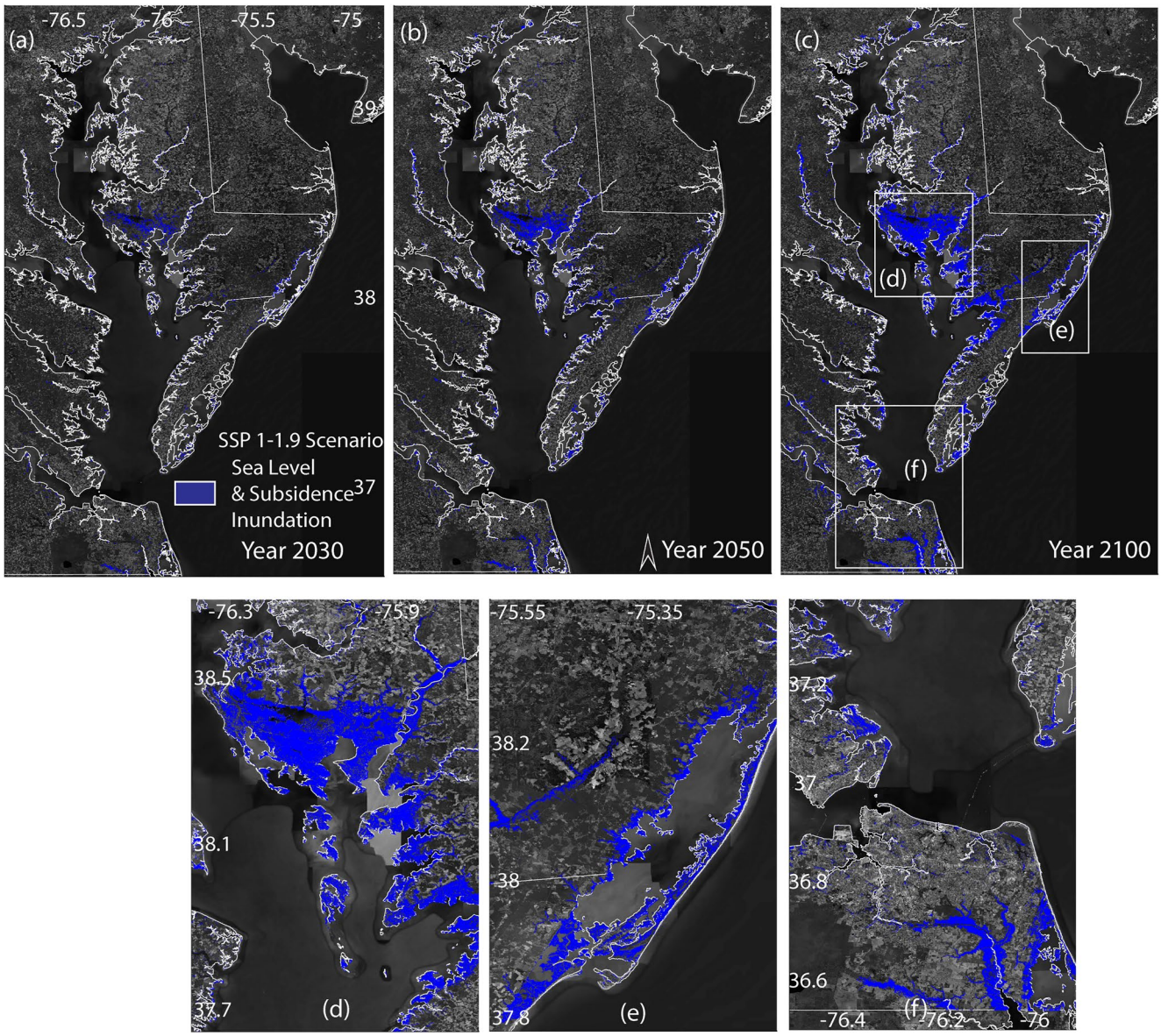

Figure 6. Projected inundation area from both subsidence and SLR under SSP 1–1.9 in years 2030, 2050, and 2100 (top panels, panels (a)–(c), respectively). The bottom panel (d)–(f) highlights zoomed-in inundation from sea level and subsidence at 2100.

lower and upper are shown in Figures S12–S14 and S15–S17 in Supporting Information S1, respectively. The inundated area from only SLR, subsidence and SLR, and including storm surge at SSPs 1–1.9, 2–4.5, and 5–8.5 likely ranges at low confidence scenarios are shown in Figure S18 in Supporting Information S1. Maps of likely lower and upper ranges of inundation projections from SLR and VLM at climate scenarios SSPs 1–2.6, 2–4.5, 5–8.5 at low confidence are shown in Figure S19–S20 in Supporting Information S1. Figure S21 in Supporting Information S1 shows projected inundation area (both upper and lower bounds) from both subsidence, SLR, and storm surge at SSP 5–8.5 for time scales 2030, 2050, and 2100 in low confidence.

We observed increased inundation areas in all five SSPs 1–1.9 to 5–8.5 for SLR (with likely ranges), ranging from 343(132–552), 410(239–570), 522(348–644), 587(474–690), and 627(526–735) km^2, respectively, in 2100 timeframe and 454(316–549), 483(401–560), 533(457–613), 571(510–651), and 600(535–690) from both SLR and VLM with 2100 time period (Figures 9a–9e and Table 1).

CB's spatial inundation maps highlight areas such as Tangier Island, Smith Island, Mockhorn Island, wetlands, and national wildlife refuges such as Blackwater national wildlife refuge and Plumtree national wildlife refuge

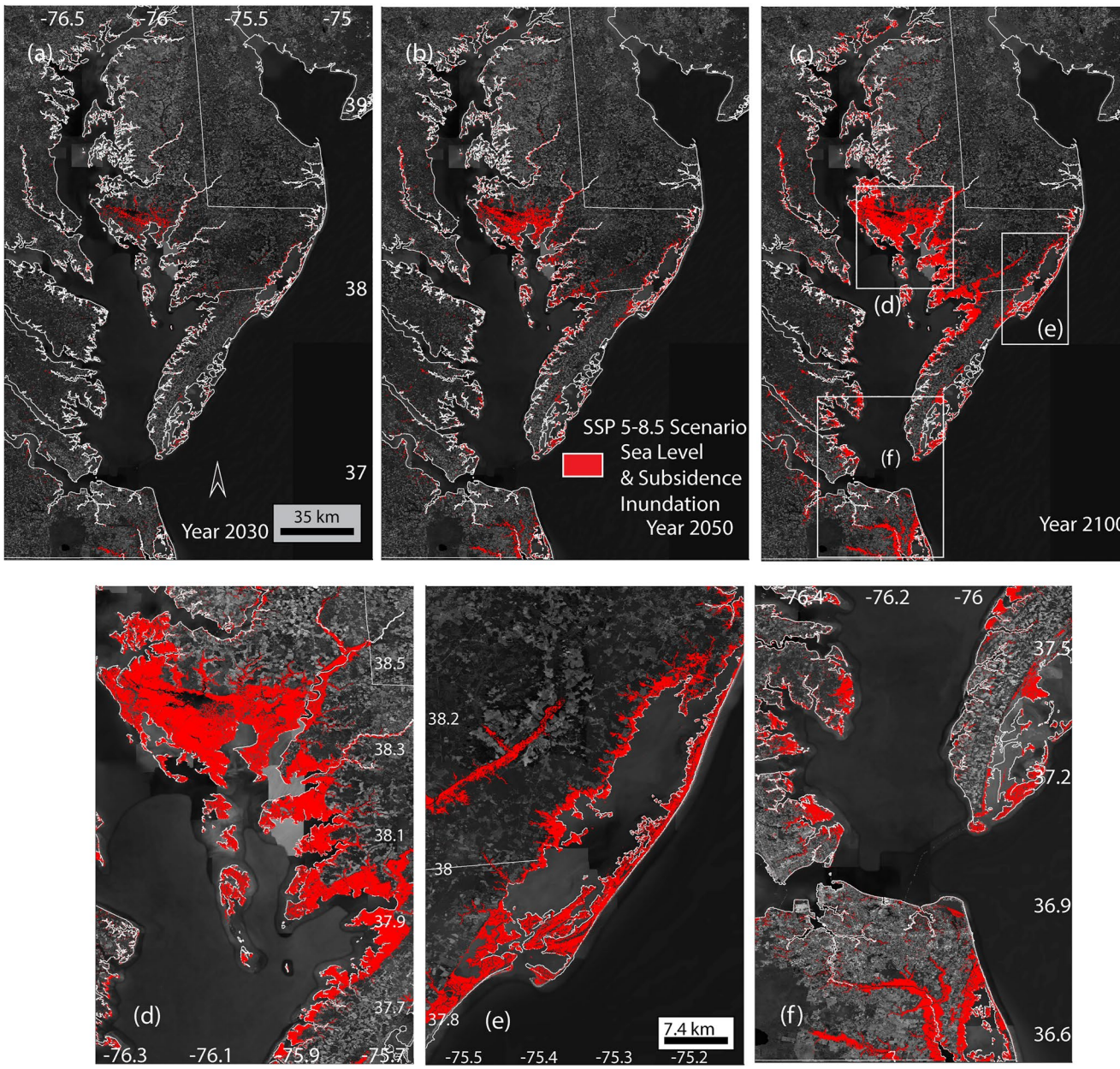

Figure 7. Projected inundation area from both subsidence and sea-level rise (SLR) at SSP 5–8.5 for time scales 2030, 2050, and 2100 (top panels, panels (a)–(c), respectively). Bottom panel (d)–(f) highlights zoomed-in inundation from sea level and subsidence in 2100.

that are flooded in even very low and low GHG emissions scenarios such as SSPs 1–1.9 to 1–2.6 (Figures 6 and S8 in Supporting Information S1). The flooded area starts extending toward mostly river channels as the climate scenarios and projection time period increase. Further, the flooded area grows toward mostly river channels as the climate scenarios and projection time period increase.

At SSP 3–7.0 and SSP 5–8.5 in 2100 time period, we observed more inundation from only SLR ranging from 587(474–690) and 627(526–735) km^2 in contrast to while including VLM effect in the projection resulting in 571(510–651) and 600(535–690) km^2 showing the result of spatially heterogenous VLM and role of uplift pixels in the overall inundation area (Figure 8 and Table 1). The combination of the storm surge scenario from Hurricane Sandy in October 2012 with the SLR showed an inundated area of 578(533–610)–1,087(1,016–1,189) km^2, respectively, from 2030 to 2100 (Figure 9f) in SSP 5–8.5 and 588(562–622)–1,232(1,160–1,338) km^2 when incorporating Hurricane Isabel of September 2003 (Figure 9g). Further, an amalgamation of all three

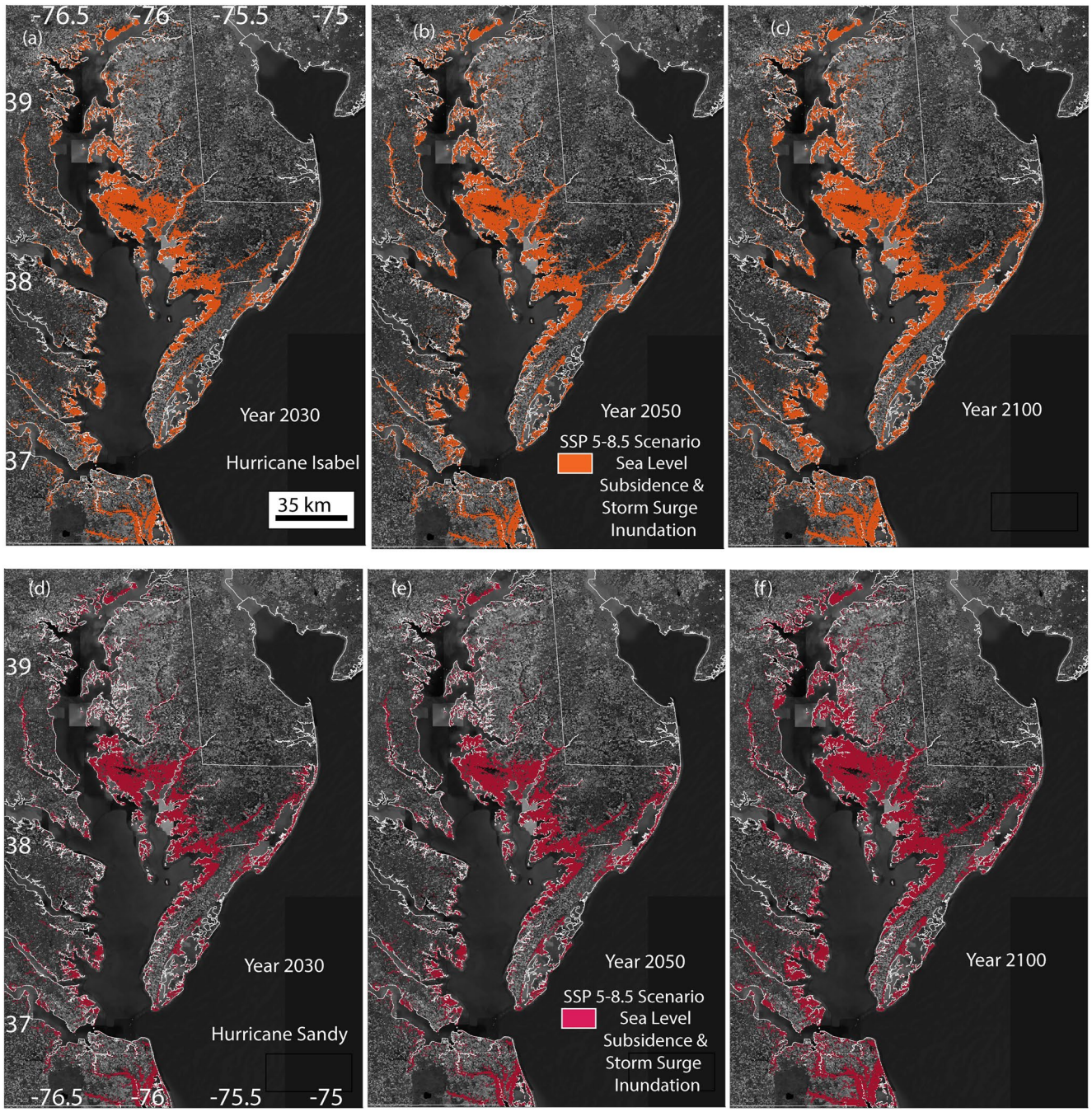

Figure 8. Projected inundation area from both subsidence, SLR, and storm surge at SSP 5–8.5 for time scales 2030, 2050, and 2100 (top panels, panels (a–c)), based on hurricane Isabel and Sandy (bottom panels (d–f)) respectively.

components SLR, VLM, and storm surge, projected inundation of 739(722–757)–1,032(943–1,090) km^2 and 849(832–867)–1,117(1,054–1,205) km^2 for Hurricanes Sandy and Isabel, respectively.

4. Discussion

The CB area, the largest estuary in the United States, is home to 15 wildlife refuges (Ernst, 2003; Ray & McCormick-Ray, 2009). The urban Hampton area encompasses the world's most extensive naval base and a dense population of >1.7 million people (DOD, 2021). Accurate estimation of VLM and flooding from sea-level

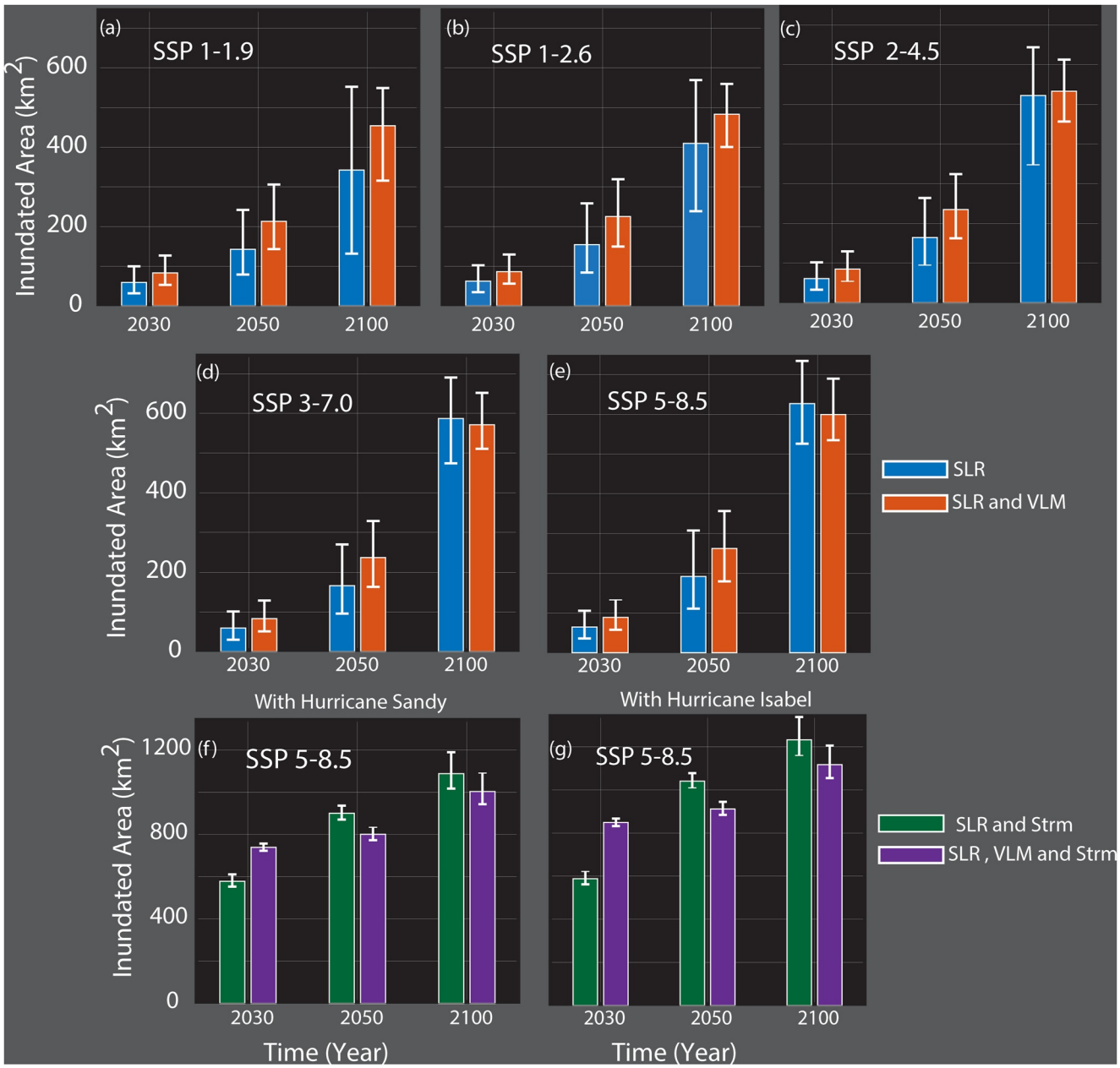

Figure 9. Inundated area from subsidence and SLR (km^2) (in orange), and only SLR (in blue in km^2) at SSPs 1–1.9, 1–2.6, 2–4.5, 3–7.0, and 5–8.5 (panels a-e), respectively, with likely upper (83%) and lower (17%) ranges. Inundation area (km^2) from storm surge based on (f) October 2012 Hurricane Sandy data sets and (g) Hurricane Isabel recorded on 18–19 September 2003 from NOAA and SLR scenario of highest emission SSP 5–8.5 in km^2 (medium confidence).

change allows flood mitigation. A recent study on the region has highlighted increasing regional sea-level changes in the CB area (Bekaert et al., 2017; Buzzanga et al., 2020; Harvey et al., 2021; Karegar et al., 2017). Here, we provide accurate high-resolution observations and estimate changes in local processes driving relative sea-level change and inundation projection until 2100, encompassing factors contributing to sea level. To perform our analysis, we assumed that the VLM rates were steady during the observation period and we ignored the gap from 2011 to 2014 between the two satellite acquisition periods. Thus, a decadal change in VLM rates may affect the estimated long-term trends. The CB region, particularly Hampton Roads, injects treated wastewater into the underlying aquifer to mitigate subsidence from aquifer compaction. A recent study by Buzzanga et al. (2020) on Hampton reported an overall subsidence rate of -3.6 ± 2.3 mm/year with considerable spatial variability and no significant effects of groundwater injection.

Table 1
Inundated Area (km²) Modeled for Five Climate Scenarios for Sea-Level Rise (SLR), SLR and Subsidence From 2030 to 2100 and SLR, Storm Surge and VLM Incorporating Hurricane Sandy of October 2012 and Hurricane Isabel of September 2003, for High Reference Scenario With No Additional Climate Policy, SSP 5–8.5 From 2030 to 2100 (Medium Confidence) Median and Likely Ranges (Lower-Upper) and for Climate Scenarios SSPs 1–2.6, 2–4.5, and 5–8.5 (Low Confidence) Likely Upper and Lower Ranges From 2030 to 2100

		Year (medium confidence)			Year (low confidence)		
		2030	2050	2100	2030	2050	2100
Content	IPCC climate scenarios	Area (km²)	Area (km²)	Area (km²)	Area (km²)	Area (km²)	Area (km²)
SLR	SSP 1–1.9	59(32–100)	143(79–242)	342(132–552)	–	–	–
	SSP 1–2.6	62(35–102)	155(84–258)	410(239–570)	(35–108)	(84–289)	(150–601)
	SSP 2–4.5	61(32–102)	164(95–264)	522(348–644)	(33–108)	(95–290)	(348–344)
	SSP 3–7.0	59(30–101)	166(96–270)	587(474–690)	–	–	–
	SSP 5–8.5	65(36–106)	192(111–307)	627(526–735)	(36–115)	(110–370)	(526–861)
SLR and subsidence	SSP 1–1.9	83(53–127)	213(143–306)	454(316–549)	–	–	–
	SSP 1–2.6	87(56–130)	225(150–320)	483(401–560)	(56–136)	(150–343)	(401–580)
	SSP 2–4.5	85(54–129)	235(162–324)	533(457–613)	(54–136)	(162–344)	(457–619)
	SSP 3–7.0	83(51–129)	237(163–328)	571(510–651)	–	–	–
	SSP 5–8.5	89(58–133)	262(180–356)	600(535–690)	(58–142)	(179–397)	(535–799)
SLR and storm surge (Hurricane Sandy)	SSP 5–8.5	578(533–610)	900(870–936)	1,087(1,016–1,189)	(553–617)	(870–956)	(1,017–1,318)
SLR, storm surge, and VLM (Hurricane Sandy)	SSP 5–8.5	739(722–757)	801(773–834)	1,032(943–1,090)	(722–760)	(773–851)	(943–1,206)
SLR and storm surge (Hurricane Isabel)	SSP 5–8.5	588(562–622)	1,041(1,009–1,078)	1,232(1,160–1,338)	(562–628)	(1,009–1,098)	(1,160–1,470)
SLR, storm surge, and VLM (Hurricane Isabel)	SSP 5–8.5	849(832–867)	911(884–944)	1,117(1,054–1,205)	(832–871)	(883–962)	(1,054–1,314)

Forward projections of VLM are crucial for assessing future flooding and inundation hazards. Following earlier studies (Fox-Kemper et al., 2021; Miller & Shirzaei, 2021; Shirzaei & Bürgmann, 2018), we considered a linear functional model for future estimates. Generally, this assumption might only be valid for the GIA effect, and most anthropogenic factors are likely nonlinear and change over time (Shirzaei et al., 2021). Despite its importance, thus far, little research has focused on scenario-based projections of coastal VLM that account for various socioeconomic and climate-forcing factors to obtain values comparable to that of SLR projections. Thus, to address this knowledge gap, new research efforts are needed to establish a link between various climate and non-climate factors and the future evolution of coastal vertical elevation.

Using a VLM-adjusted high-resolution (1-m × 1-m grid) lidar topographic data set alongside IPCC AR6 sea level scenario and two hurricanes, Sandy and Isabel, allowed estimation of flood and inundation extent in the CB throughout 21st century. For our inundation maps that incorporate storm surge, we utilized a static approach, also termed a "bathtub" (Hinkel et al., 2014), which accounts for all the areas with elevation lower than the forcing water level as flooded/inundated and do not account for coastal complexity and physical processes (infiltration and runoff) that control flooding and therefore might overestimate flooding extent, compared with hydraulic models (Ramirez et al., 2016; Vousdoukas et al., 2016). Overall, subsidence increases the hazards, except at a few locations, where some uplift is observed due to aquifer recharge and wetlands elevation gains. Even though the discussion of the drivers of subsidence and uplift is beyond the scope of this study, a study by Miller et al. (2017) has shown that 1 m groundwater level change in an aquifer with a skeletal storage coefficient of the order of 10^{-3} can create mm-level deformation, consistent with that we observed here. These results highlight the disruptive role of VLM in defending against and adapting to climate change in coastal areas.

Considering uncertainties and errors in RSL is essential for interpreting inundation hazards and risks and making relevant policy decisions. This issue has been addressed fairly well in projections of SLR. However, the projections of land elevation have not received adequate attention yet, as it is discussed in a recent review paper (Shirzaei et al., 2021). Although the errors of current estimates of coastal VLM can be quantified as standard deviation,

their projections likely underestimate future uncertainties. That is because (a) the temporal behavior of coastal VLM is poorly understood due to anthropogenic factors and (b) current errors and future changes in digital elevation models used for evaluating inundation are often unknown. We recognize that the lack of scenario-based projection of VLM and uncertainties comparable to that of SLR is the main limitation of the presented inundation models. Thus, we call for comprehensive efforts to create such projections and release them to the public together with SLR projections.

In the United States, almost 29% of the US population lives along the coastline, with >41 million people living on the Atlantic coast, including a minority population, and are vulnerable to hurricanes alongside an increase in sea level (U.S. Census Bureau, 2021). A study by Neumann et al. (2015) has projected the global coastal population to surpass 1 billion people this century. Flooding and inundation hazards can displace a large proportion of the population (Hauer et al., 2020). This further influences human migration due to permanent, irreversible inundation of low-elevation areas, which, under SLR, renders unavailable for livelihoods and ultimately land uninhabitable (Hauer et al., 2020). In Hampton Roads, flooding impacts low-income, socially vulnerable areas such as portions of Newport News, Norfolk, and Portsmouth, and some outlying rural areas in the counties of Gloucester and Surry. The most recent census data list the City of Norfolk as having 19.7% of its population living in poverty, Portsmouth as having 17.2%, and Newport News as having 15.5% (U.S. Census Bureau, 2021) and an increase in future flooding risk will disproportionately impact Black communities while remaining concentrated on the Atlantic and Gulf coasts. Our findings of current and future coastal hazards in the CB, driven by climate and solid Earth changes, provide critical information for hazard and risk management and have a significant societal relevance as they induce considerable adaptation needs for disaster resilience.

5. Conclusion

Combining ALOS and Sentinel-1 data sets with GNSS measurements, we obtained a seamless map of VLM for the period 2007–2020, indicating part of CB subside at a rate of up to −5.5 mm/year. To assess 21st-century inundation and flooding hazards due to SLR rise, storm surge, and land subsidence in the CB, we combined scenario-based SLR projections from IPCC AR6 with linear projections of VLM rates, LiDAR DEMs, and storm surges. Following include some of the main conclusions. By 2100, considering only SLR, an area of 343(132–552)–627(526–735) km^2 will be inundated under SSPs 1–1.9, 5–8.5 medium confidence scenarios. Including VLM, the inundation area increases to 454(316–549)–600(535–690) km^2 for SSPs 1–1.9, 5–8.5 medium confidence scenarios. The addition of storm surge contribution (based on Hurricane Isabel, of September 2003) to that of SLR and VLM increases the inundated area to 849(832–867)–1,117(1,054–1,205) km^2 for 2030 and 2100 for SSPs 5–8.5 medium confidence scenario. And based on Hurricane Sandy, of October 2013, increases the inundation area (from storm surge, VLM, and SLR) to 739(722–757)–1032(943–1090) km^2 from 2030 to 2100 under SSP 5–8.5 (medium confidence). In very low and low emissions scenarios, e.g., SSPs 1–1.9 and 1–2.6, Islands, wetlands, and national wildlife refuges will be flooded.

In an era of climate change and SLR, increased intensity/frequency of hurricanes will seriously threaten the coastal population, infrastructure, and ecosystem. The earth observation data, methods, and results presented here can improve the understanding of evolving hazards due to changes in the global climate-earth system, and benefits authorities, policymakers, and local communities in coastal regions.

Data Availability Statement

SAR data sets are available at the Alaska satellite facilities at https://vertex.daac.asf.alaska.edu/. GNSS velocities information is obtained from the Nevada Geodetic lab (http://geodesy.unr.edu/magnet.php). Tide gauge data sets are found on the NOAA website https://tidesandcurrents.noaa.gov/map/index.html. The LiDAR data set is a contribution from USGS and can be found at https://coast.noaa.gov/htdata/raster2/elevation/Chesapeake_Coned_update_DEM_2016_8656/. Produced inundation projections from sea-level rise (SLR), vertical land motion (VLM), and storm surge for Hurricane Isabel at climate scenarios namely Shared Socioeconomic Pathways (SSPs) 1–1.9, 1–2.6, 2–4.5, 3–7.0, and 5–8.5 at 3-time scales (2030–2050–2100) at medium confidence, median values, likely ranges upper and lower (for three selected SSPs) are available at https://doi.org/10.7294/20161580.

Acknowledgments
The work of Sonam Futi Sherpa was supported by the US Geological Survey and NASA Grant 80NSSC170567 and in part by the National Science Foundation under Grant 1735139. Any opinions, findings, and conclusions, or recommendations expressed in this material are those of the authors and do not necessarily reflect the views of the National Science Foundation. Manoochehr Shirzaei was supported by the US Geological Survey and partially by NASA Grant 80NSSC170567. The support of the Geological Society of America (GSA) is acknowledged here. We thank the projection authors for developing and making the SLR projections available, multiple funding agencies for supporting the development of the projections, and the NASA Sea-Level Change Team for developing and hosting the IPCC AR6 Sea-Level Projection Tool.

References

Allen, M. J., & Allen, T. R. (2019). Precipitation trends across the Commonwealth of Virginia (1947–2016). *Virginia Journal of Science*, *70*(1), 4. https://doi.org/10.25778/3cay-z849

Arias, P. A., Bellouin, N., Coppola, E., Jones, R. G., Krinner, G., Marotzke, J., et al. (2021). Technical summary. In V. Masson-Delmotte, P. Zhai, A. Pirani, S. L. Connors, C. Péan, S. Berger, et al. (Eds.), *Climate change 2021: The physical science basis. Contribution of Working Group I to the Sixth Assessment Report of the Intergovernmental Panel on Climate Change* (pp. 33–144). Cambridge University Press. https://doi.org/10.1017/9781009157896.002

Bekaert, D. P. S., Hamlington, B. D., Buzzanga, B., & Jones, C. E. (2017). Spaceborne synthetic aperture radar survey of subsidence in Hampton Roads, Virginia (USA). *Scientific Reports*, *7*(1), 14752. https://doi.org/10.1038/s41598-017-15309-5

Blackwell, E., Shirzaei, M., Ojha, C., & Werth, S. (2020). Tracking California's sinking coast from space: Implications for relative sea-level rise. *Science Advances*, *6*(31), eaba4551. https://doi.org/10.1126/sciadv.aba4551

Blake, E. S., Kimberlain, T. B., Berg, R. J., Cangialosi, J. P., & Beven, J. L. (2013). *Tropical cyclone report Hurricane Sandy (AL182012) 22–29 October 2012*. National Hurricane Center.

Boon, J., Brubaker, J., & Forrest, D. (2010). *Chesapeake Bay land subsidence and sea level change: An evaluation of past and present trends and future outlook (Report 425)*. Virginia Institute of Marine Science, William & Mary. https://doi.org/10.21220/V58X4P

Boon, J. D. (2018). *Anthropocene Sea level change: A history of recent trends observed in the U.S. East, Gulf, and west coast regions (No. 467)*. Virginia Institute of Marine Science, William & Mary. https://doi.org/10.21220/V5T17T

Bürgmann, R., Rosen, P. A., & Fielding, E. J. (2000). Synthetic aperture radar interferometry to measure Earth's surface topography and its deformation. *Annual Review of Earth and Planetary Sciences*, *28*(1), 169–209. https://doi.org/10.1146/annurev.earth.28.1.169

Buzzanga, B., Bekaert, D. P. S., Hamlington, B. D., & Sangha, S. S. (2020). Toward sustained monitoring of subsidence at the coast using InSAR and GPS: An application in Hampton Roads, Virginia. *Geophysical Research Letters*, *47*, e2020GL090013. https://doi.org/10.1029/2020GL090013

Chen, Q., van Dam, T., Sneeuw, N., Collilieux, X., Weigelt, M., & Rebischung, P. (2013). Singular spectrum analysis for modeling seasonal signals from GPS time series. *Journal of Geodynamics*, *72*, 25–35. https://doi.org/10.1016/j.jog.2013.05.005

Cho, K.-H., Wang, H. V., Shen, J., Valle-Levinson, A., & Teng, Y. (2012). A modeling study on the response of Chesapeake Bay to hurricane events of Floyd and Isabel. *Ocean Modelling*, *49*(50), 22–46. https://doi.org/10.1016/j.ocemod.2012.02.005

Dangendorf, S., Hay, C., Calafat, F. M., Marcos, M., Piecuch, C. G., Berk, K., & Jensen, J. (2019). Persistent acceleration in global sea-level rise since the 1960s. *Nature Climate Change*, *9*(9), 705–710. https://doi.org/10.1038/s41558-019-0531-8

Davis, J. L., & Vinogradova, N. T. (2017). Causes of accelerating sea level on the East Coast of North America. *Geophysical Research Letters*, *44*, 5133–5141. https://doi.org/10.1002/2017GL072845

DOD. (2021). Navy Confront climate change challenges in southern Virginia. Retrieved from https://www.defense.gov/News/News-Stories/Article/Article/2703096/dod-navy-confront-climate-change-challenges-in-southern-virginia/

Eggleston, J., & Pope, J. (2013). *Land subsidence and relative sea-level rise in the southern Chesapeake Bay region (Circular No. 1392)* (p. 30). U.S. Geological Survey. https://doi.org/10.3133/cir1392

Ernst, H. R. (2003). *Chesapeake Bay blues: Science, politics, and the struggle to save the bay*. Rowman & Littlefield.

Ezer, T., & Corlett, W. B. (2012). Is sea level rise accelerating in the Chesapeake Bay? A demonstration of a novel new approach for analyzing sea level data. *Geophysical Research Letters*, *39*, L19605. https://doi.org/10.1029/2012GL053435

Fanelli, C., Fanelli, P., & Wolcott, D. (2013). *Hurricane Sandy (NOAA Water Level and Meteorological Data Report)*. National Oceanic and Atmospheric Administration, US Department of Commerce. Retrieved from https://tidesandcurrents.noaa.gov/publications/Hurricane_Sandy_2012_Water_Level_and_Meteorological_Data_Report.pdf

Fox-Kemper, B., Hewitt, H. T., Aðalgeirsdóttir, G., Drijfhout, S. S., Edwards, T. L., Golledge, N. R., et al. (2021). Ocean, cryosphere and sea level change. In V. Masson-Delmotte, P. Zhai, A. Pirani, S. L. Connors, C. Péan, S. Berger, et al. (Eds.), *Climate Change 2021: The Physical Science Basis. Contribution of working Group I to the Sixth Assessment Report of the Intergovernmental Panel on Climate Change* (pp. 1211–1362). Cambridge University Press. https://doi.org/10.1017/9781009157896.011

Frederikse, T., Landerer, F., Caron, L., Adhikari, S., Parkes, D., Humphrey, V. W., et al. (2020). The causes of sea-level rise since 1900. *Nature*, *584*(7821), 393–397. https://doi.org/10.1038/s41586-020-2591-3

Garner, G. G., Hermans, T., Kopp, R. E., Slangen, A. B. A., Edwards, T. L., Levermann, S., et al. (2021). *IPCC AR6 sea-level rise projections. Version 20210809*. PO.DAAC.

Gill, S. K., & Schultz, J. R. (2001). *Tidal datums and their applications* (Report). NOAA, NOS Center for Operational Oceanographic Products and Services. https://doi.org/10.25607/OBP-170

Harvey, T. C., Hamlington, B. D., Frederikse, T., Nerem, R. S., Piecuch, C. G., Hammond, W. C., et al. (2021). Ocean mass, sterodynamic effects, and vertical land motion largely explain US coast relative sea level rise. *Communications Earth & Environment*, *2*(1), 233. https://doi.org/10.1038/s43247-021-00300-w

Hauer, M. E., Fussell, E., Mueller, V., Burkett, M., Call, M., Abel, K., et al. (2020). Sea-level rise and human migration. *Nature Reviews Earth & Environment*, *1*(1), 28–39. https://doi.org/10.1038/s43017-019-0002-9

Hinkel, J., Lincke, D., Vafeidis, A. T., Perrette, M., Nicholls, R. J., Tol, R. S. J., et al. (2014). Coastal flood damage and adaptation costs under 21st century sea-level rise. *Proceedings of the National Academy of Sciences of the United States of America*, *111*(9), 3292–3297. https://doi.org/10.1073/pnas.1222469111

Homer, C. G., Fry, J. A., & Barnes, C. A. (2012). The national land cover database (No. 2012-3020). Fact sheet. *U.S. Geological Survey*. https://doi.org/10.3133/fs20123020

Hovis, J., Popovich, W., Zervas, C., Hubbard, J., Shih, H. H., & Stone, P. (2004). *Effects of Hurricane Isabel on water levels data report* (Technical Report, p. 120). National Oceanic and Atmospheric Administration, US Department of Commerce. Retrieved from https://tidesandcurrents.noaa.gov/publications/techrpt40.pdf

IPCC. (2021). Summary for policymakers. In V. Masson-Delmotte, P. Zhai, A. Pirani, S. L. Connors, C. Péan, et al. (Eds.), *Climate change 2021: The physical Science Basis. Contribution of Working Group I to the Sixth Assessment Report of the Intergovernmental Panel on Climate Change* (pp. 3–32). Cambridge University Press. https://doi.org/10.1017/9781009157896.001

Jankowski, K. L., Törnqvist, T. E., & Fernandes, A. M. (2017). Vulnerability of Louisiana's coastal wetlands to present-day rates of relative sea-level rise. *Nature Communications*, *8*(1), 14792. https://doi.org/10.1038/ncomms14792

Karegar, M. A., Dixon, T. H., & Engelhart, S. E. (2016). Subsidence along the Atlantic Coast of North America: Insights from GPS and late Holocene relative sea level data. *Geophysical Research Letters*, *43*, 3126–3133. https://doi.org/10.1002/2016GL068015

Karegar, M. A., Dixon, T. H., Malservisi, R., Kusche, J., & Engelhart, S. E. (2017). Nuisance flooding and relative sea-level rise: The importance of present-day land motion. *Scientific Reports*, *7*(1), 11197. https://doi.org/10.1038/s41598-017-11544-y

Lee, J.-C., & Shirzaei, M. (2023). Novel algorithms for pair and pixel selection and atmospheric error correction in multitemporal InSAR. *Remote Sensing of Environment*, *286*, 113447. https://doi.org/10.1016/j.rse.2022.113447

Lin, N., Emanuel, K., Oppenheimer, M., & Vanmarcke, E. (2012). Physically based assessment of hurricane surge threat under climate change. *Nature Climate Change*, *2*(6), 462–467. https://doi.org/10.1038/nclimate1389

McFarland, R. E., & Scott, B. T. (2006). *The Virginia coastal plain hydrogeologic framework*. Virginia Water Science Center. https://doi.org/10.3133/pp1731

Miller, M. M., & Shirzaei, M. (2021). Assessment of future flood hazards for southeastern Texas: Synthesizing subsidence, sea-level rise, and storm surge scenarios. *Geophysical Research Letters*, *48*, e2021GL092544. https://doi.org/10.1029/2021GL092544

Miller, M. M., Shirzaei, M., & Argus, D. (2017). Aquifer mechanical properties and decelerated compaction in Tucson, Arizona. *Journal of Geophysical Research: Solid Earth*, *122*, 8402–8416. https://doi.org/10.1002/2017JB014531

Nerem, R. S., Beckley, B. D., Fasullo, J. T., Hamlington, B. D., Masters, D., & Mitchum, G. T. (2018). Climate-change-driven accelerated sea-level rise detected in the altimeter era. *Proceedings of the National Academy of Sciences of the United States of America*, *115*(9), 2022–2025. https://doi.org/10.1073/pnas.1717312115

Neumann, B., Vafeidis, A. T., Zimmermann, J., & Nicholls, R. J. (2015). Future coastal population growth and exposure to sea-level rise and coastal flooding—A global assessment. *PLoS One*, *10*(3), e0118571. https://doi.org/10.1371/journal.pone.0118571

OCM Partners. (2021). *2016 USGS CoNED topobathymetric model (1859–2015): Chesapeake bay region from 2010-06-15 to 2010-08-15*. NOAA National Centers for Environmental Information. Retrieved from https://www.fisheries.noaa.gov/inport/item/55321

O'Neill, B. C., Kriegler, E., Riahi, K., Ebi, K. L., Hallegatte, S., Carter, T. R., et al. (2014). A new scenario framework for climate change research: The concept of shared socioeconomic pathways. *Climatic Change*, *122*(3), 387–400. https://doi.org/10.1007/s10584-013-0905-2

Peltier, W. R., Argus, D. F., & Drummond, R. (2018). Comment on "An assessment of the ICE-6G_C (VM5a) glacial isostatic adjustment model" by Purcell et al. *Journal of Geophysical Research: Solid Earth*, *123*, 2019–2028. https://doi.org/10.1002/2016JB013844

Ramirez, J. A., Lichter, M., Coulthard, T. J., & Skinner, C. (2016). Hyper-resolution mapping of regional storm surge and tide flooding: Comparison of static and dynamic models. *Natural Hazards*, *82*(1), 571–590. https://doi.org/10.1007/s11069-016-2198-z

Ray, G. C., & McCormick-Ray, J. (2009). *Coastal-marine conservation: Science and policy*. John Wiley & Sons.

Riahi, K., van Vuuren, D. P., Kriegler, E., Edmonds, J., O'Neill, B. C., Fujimori, S., et al. (2017). The Shared Socioeconomic Pathways and their energy, land use, and greenhouse gas emissions implications: An overview. *Global Environmental Change*, *42*, 153–168. https://doi.org/10.1016/j.gloenvcha.2016.05.009

Sallenger, A. H., Doran, K. S., & Howd, P. A. (2012). Hotspot of accelerated sea-level rise on the Atlantic coast of North America. *Nature Climate Change*, *2*(12), 884–888. https://doi.org/10.1038/nclimate1597

Sella, G. F., Stein, S., Dixon, T. H., Craymer, M., James, T. S., Mazzotti, S., & Dokka, R. K. (2007). Observation of glacial isostatic adjustment in "stable" North America with GPS. *Geophysical Research Letters*, *34*, L02306. https://doi.org/10.1029/2006GL027081

Shen, J., Wang, H., Sisson, M., & Gong, W. (2006). Storm tide simulation in the Chesapeake Bay using an unstructured grid model. *Estuarine, Coastal and Shelf Science*, *68*(1), 1–16. https://doi.org/10.1016/j.ecss.2005.12.018

Sheng, Y. P., Alymov, V., & Paramygin, V. A. (2010). Simulation of storm surge, wave, currents, and inundation in the Outer Banks and Chesapeake Bay during Hurricane Isabel in 2003: The importance of waves. *Journal of Geophysical Research*, *115*, C04008. https://doi.org/10.1029/2009JC005402

Shirzaei, M. (2013). A wavelet-based multitemporal DInSAR algorithm for monitoring ground surface motion. *IEEE Geoscience and Remote Sensing Letters*, *10*(3), 456–460. https://doi.org/10.1109/LGRS.2012.2208935

Shirzaei, M., & Bürgmann, R. (2018). Global climate change and local land subsidence exacerbate inundation risk to the San Francisco Bay Area. *Science Advances*, *4*(3), eaap9234. https://doi.org/10.1126/sciadv.aap9234

Shirzaei, M., Bürgmann, R., & Fielding, E. J. (2017). Applicability of Sentinel-1 Terrain Observation by Progressive Scans multitemporal interferometry for monitoring slow ground motions in the San Francisco Bay area. *Geophysical Research Letters*, *44*, 2733–2742. https://doi.org/10.1002/2017GL072663

Shirzaei, M., Freymueller, J., Törnqvist, T. E., Galloway, D. L., Dura, T., & Minderhoud, P. S. J. (2021). Measuring, modelling and projecting coastal land subsidence. *Nature Reviews Earth & Environment*, *2*(1), 40–58. https://doi.org/10.1038/s43017-020-00115-x

Smith, C. M., & Graffeo, C. S. (2005). Regional impact of Hurricane Isabel on emergency departments in coastal southeastern Virginia. *Academic Emergency Medicine*, *12*(12), 1201–1205. https://doi.org/10.1197/j.aem.2005.06.024

Sopkin, K. L., Stockdon, H. F., Doran, K. S., Plant, N. G., Morgan, K. L. M., Guy, K. K., & Smith, K. E. L. (2014). *Hurricane Sandy: Observations and analysis of coastal change (No. 2014-1088)*. *Open-File Report*. U.S. Geological Survey. https://doi.org/10.3133/ofr20141088

Sweet, W. V., & Park, J. (2014). From the extreme to the mean: Acceleration and tipping points of coastal inundation from sea level rise. *Earth's Future*, *2*, 579–600. https://doi.org/10.1002/2014EF000272

U.S. Census Bureau. (2021). U.S. Census Bureau QuickFacts: Portsmouth city, Virginia; Newport news city, Virginia; Norfolk city, Virginia; Virginia. Retrieved from https://www.census.gov/quickfacts/fact/table/portsmouthcityvirginia,newportnewscityvirginia,norfolkcityvirginia,VA/IPE120219

Vousdoukas, M. I., Voukouvalas, E., Mentaschi, L., Dottori, F., Giardino, A., Bouziotas, D., et al. (2016). Developments in large-scale coastal flood hazard mapping. *Natural Hazards and Earth System Sciences*, *16*(8), 1841–1853. https://doi.org/10.5194/nhess-16-1841-2016

Wegnüller, U., Werner, C., Strozzi, T., Wiesmann, A., Frey, O., & Santoro, M. (2016). Sentinel-1 support in the GAMMA software. *Procedia Computer Science*, *100*, 1305–1312. https://doi.org/10.1016/j.procs.2016.09.246

Werner, C., Wegmüller, U., Strozzi, T., & Wiesmann, A. (2000). Gamma SAR and interferometric processing software. In *Proceedings of the ERS-ENVISAT Symposium Gothenburg, Sweden* (Vol. 1620, p. 1620).

Zhang, K., Douglas, B. C., & Leatherman, S. P. (2004). Global warming and coastal erosion. *Climatic Change*, *64*(1), 41–58. https://doi.org/10.1023/B:CLIM.0000024690.32682.48

Zoccarato, C., Minderhoud, P. S. J., & Teatini, P. (2018). The role of sedimentation and natural compaction in a prograding delta: Insights from the mega Mekong delta, Vietnam. *Scientific Reports*, *8*(1), 11437. https://doi.org/10.1038/s41598-018-29734-7

References From the Supporting Information

Blewitt, G., Hammond, W. C., & Kreemer, C. (2018). Harnessing the GPS data explosion for interdisciplinary science. *Eos*, *99*, 485. https://doi.org/10.1029/2018EO104623

Costantini, M. (1998). A novel phase unwrapping method based on network programming. *IEEE Transactions on Geoscience and Remote Sensing*, *36*(3), 813–821. https://doi.org/10.1109/36.673674

Costantini, M., & Rosen, P. A. (1999). A generalized phase unwrapping approach for sparse data. In *IEEE 1999 International Geoscience and Remote Sensing Symposium IGARSS'99 (Cat. No. 99CH36293)* (Vol. 1, pp. 267–269). https://doi.org/10.1109/IGARSS.1999.773467

Franceschetti, G., & Lanari, R. (1999). *Synthetic aperture radar processing. Electronic engineering systems series*. CRC Press.

Hammond, W. C., Blewitt, G., & Kreemer, C. (2016). GPS imaging of vertical land motion in California and Nevada: Implications for Sierra Nevada uplift. *Journal of Geophysical Research: Solid Earth*, *121*, 7681–7703. https://doi.org/10.1002/2016JB013458

Hanssen, R. F. (2001). *Radar interferometry: Data interpretation and error analysis* (Vol. 2). Springer Science & Business Media.

Liang, C., Agram, P., Simons, M., & Fielding, E. J. (2019). Ionospheric correction of InSAR time series analysis of C-band Sentinel-1 TOPS data. *IEEE Transactions on Geoscience and Remote Sensing*, *57*(9), 6755–6773. https://doi.org/10.1109/TGRS.2019.2908494

Ojha, C., Shirzaei, M., Werth, S., Argus, D. F., & Farr, T. G. (2018). Sustained groundwater loss in California's Central Valley exacerbated by intense drought periods. *Water Resources Research*, *54*, 4449–4460. https://doi.org/10.1029/2017WR022250

Pulliainen, J. T., Kurvonen, L., & Hallikainen, M. T. (1999). Multitemporal behavior of L- and C-band SAR observations of boreal forests. *IEEE Transactions on Geoscience and Remote Sensing*, *37*(2), 927–937. https://doi.org/10.1109/36.752211

Shirzaei, M., & Bürgmann, R. (2012). Topography correlated atmospheric delay correction in radar interferometry using wavelet transforms. *Geophysical Research Letters*, *39*, L01305. https://doi.org/10.1029/2011GL049971

Shirzaei, M., & Walter, T. R. (2011). Estimating the effect of satellite orbital error using wavelet-based robust regression applied to InSAR deformation data. *IEEE Transactions on Geoscience and Remote Sensing*, *49*(11), 4600–4605. https://doi.org/10.1109/tgrs.2011.2143419

Trochu, F. (1993). A contouring program based on dual kriging interpolation. *Engineering with Computers*, *9*(3), 160–177. https://doi.org/10.1007/BF01206346

Wauthier, C., Oyen, A. M., Marinkovic, P. S., Cayol, V., Fernandez, J., Gonzalez, P., et al. (2009). L-band and C-band InSAR studies of African volcanic areas. In *2009 IEEE International Geoscience and Remote Sensing Symposium* (Vol. 2, pp. II-210–II–213). https://doi.org/10.1109/IGARSS.2009.5418043